

Metal Coordination Determines the Catalytic Activity of IrO₂ Nanoparticles for the Oxygen Evolution Reaction

Danilo González,^a Mariona Sodupe,^a Luis Rodríguez-Santiago,^a

Xavier Solans-Monfort^{*,a}

Departament de Química, Universitat Autònoma de Barcelona,

08193 Bellaterra, Spain

ABSTRACT

H₂ production through water electrolysis is a promising strategy for storing sunlight energy. For the oxygen evolution reaction, iridium oxide containing materials are state-of-the-art due to their stability in acidic conditions. Moreover, precious metal content can be reduced by using small nanoparticles that show high catalytic activities. We performed DFT calculations on a 1.2 nm large IrO₂ Wulff-like stoichiometric nanoparticle model (IrO₂) with the aim of determining the factors controlling the catalytic activity of IrO₂ nanoparticles. Results show that at reaction conditions tetra- and tricoordinated iridium centers are not fully oxidized, the major species being IrO(OH) and IrO(OH)₂, respectively. Moreover, the computed overpotentials show that low coordinated iridium centers are more active than the pentacoordinated sites of the well-defined facets. These low coordination sites are likely more abundant on amorphous nanoparticles, which could be one of the factors explaining the higher catalytic activity observed for non-crystalline materials.

KEYWORDS: Water electrolysis, Oxygen Evolution Reaction, iridium oxide, nanoparticles, DFT

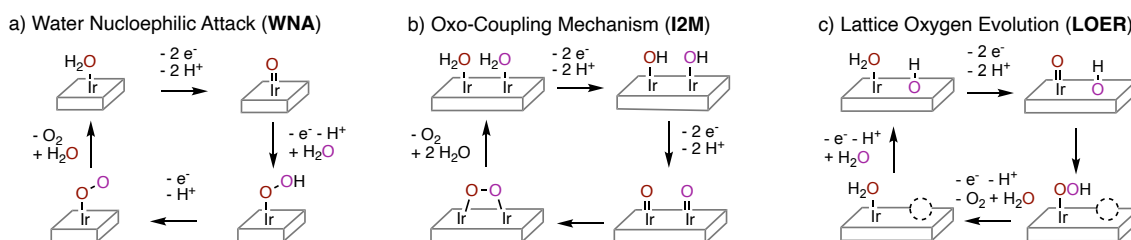
1. INTRODUCTION

The use of H₂ as sunlight energy storing source is seen as one of the most promising strategies for obtaining clean energy.[1,2] This can be achieved through the (photo)electrochemical splitting of water that converts water in oxygen at the anode through the oxygen evolution reaction (OER) and H₂ at the cathode by means of the hydrogen evolution reaction (HER).[3–9] The OER is a four-electron process that presents high overpotentials and slow kinetics and is considered the limiting half reaction for the application of water electrolysis as source for sustainable energy conversion and storage.[10–12] Several OER promising catalysts have been reported in the literature.[13,14] Within the large list of catalytically active species, IrO₂ is considered to be the most efficient one in acidic media due to both its catalytic activity and stability in harsh reaction conditions.[11,12,15]

Iridium is an expensive precious metal and consequently lowering the iridium content on the catalyst is an essential issue for the practical implementation of the water splitting.[15–20] Several research groups have synthesized small IrO₂(IrO_x) nanoparticles of different sizes and shapes showing high intrinsic activities that become remarkably high when normalizing by the catalyst amount.[21,22,31–33,23–30] Indeed, nanoparticles of about 1.5 – 2.0 nm have been shown to be within the most active species,[21,23,26,29,30] the origin of their high activity being associated to three factors: i) The Ir(III)/Ir(IV) ratio; ii) The amount of surface hydroxylated species and iii) The degree of amorphization.

Three main reaction mechanisms have been proposed for the OER (Scheme 1):[10,11,34–37] i) the water nucleophilic attack (WNA) in which the O-O bond of O₂ is

formed by the reaction of an Ir=O species of the surface and a water molecule of the solution; ii) the oxo-coupling mechanism (I2M) in which the O-O bond is formed by the coupling of two Ir=O species on the surface and iii) the lattice oxygen evolution reaction mechanism (LOER) that involve oxygen atoms from the material in the O₂ formation. The latter has been proposed to be important in amorphous materials, but less important in crystalline rutile-like materials.[11,38] Indeed, for crystalline IrO₂, the WNA pathway is the most accepted mechanism, except in very flexible environments, where the I2M mechanism becomes competitive.[39,40] Indeed, the local morphology of the material seems to tune the catalytic activity of IrO₂ for OER.[41–44]



Scheme 1.

From a computational point of view, the catalytic activity of iridium-based materials for the OER has been addressed either with slab models of the (110) surface[39,45,54–56,46–53] or small clusters up to 13 Ir centers.[57,58] Regarding the studies with slab models, most contributions limit the study to the thermodynamic cost of each PCET step. Only in a few cases, the energy barriers associated with some of the elementary steps have been computed (mostly the chemical ones) and the associated energy barriers tend to be low,[49,50,53,55,56] thus suggesting that the thermodynamics of the PCET is sufficient to get overpotential trends. Moreover, while most of these

contributions agree that the most favorable mechanism on the (110) surface is the WNA, some discrepancies exist on the nature of the overpotential defining step. Indeed, three different steps have been proposed to be rate limiting depending on the level of theory used and the definition of the elementary steps of the reaction: i) the Ir-OH to Ir-O oxidation; ii) the electrochemical step associated with the Ir-OOH intermediate formation and iii) the O₂ release. On the other hand, regarding the OER on cluster models, Auer and co-workers analyzed the effect of the applied potential and pH on the structure of two models containing either 3 or 13 iridium centers.[58] Results for the larger cluster show that at acidic reaction conditions the surface presents mainly Ir-O and Ir-OH groups, the number of Ir-OH decreasing when increasing the applied potential and the pH. Moreover, the O-O bond formation through the WNA mechanism is predicted to present a non-negligible energy barrier that decreases while increasing the applied potential.

Remarkably, nanoparticles, even being crystalline, present particular sites such as tips, edges and corners whose representation with extended models may not be appropriate, even if other surfaces other than the (110) are taken into account.[56] In addition, clusters may not properly represent the electronic structure of the commonly used nanoparticle sizes. In this contribution, we address the OER reaction on all potentially active sites present in the stoichiometric Wulff-like (IrO₂)₃₃ nanoparticle model. Results show that the oxygen evolution reaction on tri- and tetraordinated iridium centers presents lower overpotentials than on pentacoordinated sites. This is associated with the presence of Ir(OH)_n species at reaction conditions. These low coordinated sites are likely more abundant in amorphous materials, thus giving a potential explanation on the high

catalytic activity of non-crystalline IrO₂ and its dependence with the presence of Ir(OH)_n species on the surface.

2. COMPUTATIONAL DETAILS

Wulff-like stoichiometric nanoparticle models of 1.2 nm size were constructed with the BCN-M computational tool (Figure 1).[59] The surface energies provided to construct the model are 0.150, 0.158, 0.185 and 0.206 eV Å⁻² for the (110), (011), (100) and (001) crystallographic surfaces,[60] respectively. The final model size is close to some of the experimentally reported active nanoparticles,[21,23,26,29,30] and it is computationally affordable. The initial BCN-M model (Ir₃₃O₆₆) contains 33 IrO₂ units and it was relaxed adding to all unsaturated iridium vacant sites one water molecule. This allows to better describe the aqueous environment in which IrO₂ nanoparticles are usually synthesized and avoid unrealistic reconstructions.[61] After full optimization, the added water molecules were removed, and all nanoparticle atoms, except the singly coordinated oxygen atoms, were kept fix in all subsequent calculations.

At reaction conditions, it is expected that the nanoparticle would be highly oxidized, thus presenting several Ir-OH and Ir=O groups at the vacant sites of the surface iridium atoms. Inclusion of these groups in each iridium center in combination with the spin polarized formalism makes SCF convergence challenging and thus, we only considered the oxidation of the iridium centers involved in the reaction, which requires the presence of two Ir-O groups. One of the two Ir-O centers acts as the active site and the neighbor one either actively participate in the oxo-coupling mechanism or it assists the chemical water nucleophilic attack step. Noteworthy, for surface models, this approach

leads to overpotentials that are similar to those computed when considering a full surface oxidation,[56] and thus present methodology should be sufficient to get reactivity trends between the different sites.

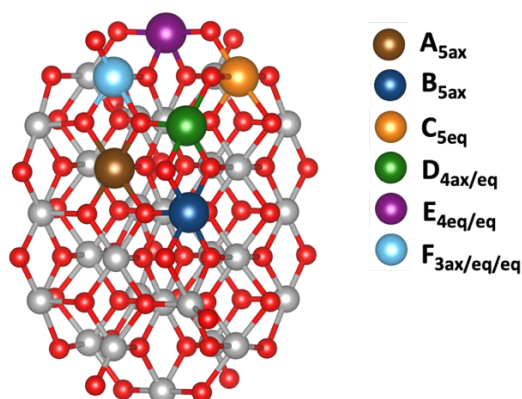


Figure 1. $(\text{IrO}_2)_{33}$ nanoparticle model with the undercoordinated iridium centers (coloured atoms) where OER activity has been studied.

All calculations were performed with the VASP code,[62,63] using the spin polarized formalism, the PBE density functional[64] and the Grimme's D2 empirical correction to account for dispersion forces.[65] PBE functional has been widely used in modeling the OER with iridium based materials including finite clusters[39,40,49,50,52,56,58] and according to Goddard and co-workers represents the metallic nonmagnetic electronic structure of the bulk in better agreement with experiments than hybrid functionals or the PBE-U approach.[66] PAW pseudopotentials were used to describe the ionic cores.[67,68] The valence electrons were represented with a plane wave basis with a kinetic energy cutoff of 500 eV. Moreover, single point calculations at the final optimized geometries were performed to include solvent effects (water, $\epsilon = 80.0$) with VASPsol

package.[69] The nanoparticle model was placed in a cubic box of a 30 Å edge and the calculations were performed at gamma point due to the model dimensionality.

Since the global process has been experimentally determined to be endothermic by 4.92 eV and it implies four PCET, an ideal electrocatalyst should catalyze these reactions at potentials of 1.23 V. Therefore, the minimum required overpotential (η^{OER}) is computed as the ΔG° difference between the highest in Gibbs energy PCET process and 1.23 V and it is used to determine the most active sites. Note that the reaction energy is imposed to be 4.92 eV due to the way the G° of O_2 is computed (see below).

$$\eta^{\text{OER}} = \max[\Delta G^\circ(\text{PCET})]/e^- - 1.23 \quad (1)$$

Values reported along the text are based on Gibbs energies at 1 atm and $T = 273.15$ K assuming the computational standard hydrogen electrode for the proton coupled electron transfer steps (PCET).[45,70] Thermal contributions were computed through different approximations: i) For the OER intermediates, the thermal corrections were obtained by considering the contributions to the vibrational modes of the adsorbed species and the Ir- O_{ads} stretching mode; ii) The entropy term of H_2O and H_2 were taken from tabulated values for liquid H_2O and H_2 gas, respectively; and iii) In analogy with previous contributions,[39,45,50] the O_2 Gibbs energy (in eV) was computed as $4.92 + 2G_{\text{H}_2\text{O}}^0 - 2G_{\text{H}_2}^0$ where 4.92 is the experimental reaction energy and $G_{\text{H}_2\text{O}}^0$ and $2G_{\text{H}_2}^0$ are the computed Gibbs energies for water and hydrogen, respectively.

3. RESULTS AND DISCUSION

We have studied the catalytic activity for the oxygen evolution reaction of the six different undercoordinated iridium centers present in the $(\text{IrO}_2)_{33}$ nanoparticle (Figure 1): **A_{5ax}** (brown), **B_{5ax}** (dark blue), **C_{5eq}** (orange), **D_{4ax/eq}** (green), **E_{4eq/eq}** (purple) and **F_{3ax/eq/eq}** (light blue). The six centers differ on the coordination number and environment. Taking into account that iridium in rutile shows two short Ir-O axial distances and four long equatorial ones,[60] the six centers can be divided in five different types: i) pentacoordinated atoms with an axial vacant site (**A_{5ax}** and **B_{5ax}**); ii) pentacoordinated sites with an equatorial vacancy (**C_{5eq}**); iii) tetracoordinated centers with one axial and one equatorial vacant site (**D_{4ax/eq}**); iv) tetracoordinated sites with two equatorial vacant sites (**E_{4eq/eq}**); and v) iridium centers presenting only three bonds with lattice oxygens (**F_{3ax/eq/eq}**). While other sites exist in larger Wulff-like nanoparticle models, they can all be classified in one of these five types of centers.[59,61] Indeed, we found that the water adsorption in the existing sites of $(\text{IrO}_2)_{33}$ and $(\text{IrO}_2)_{115}$ nanoparticle models is mainly determined by the nature of the vacant site and nanoparticle morphology and not by the nanoparticle size.[61] Therefore, the results reported here should be indicative of how the different sites of the nanoparticle react.

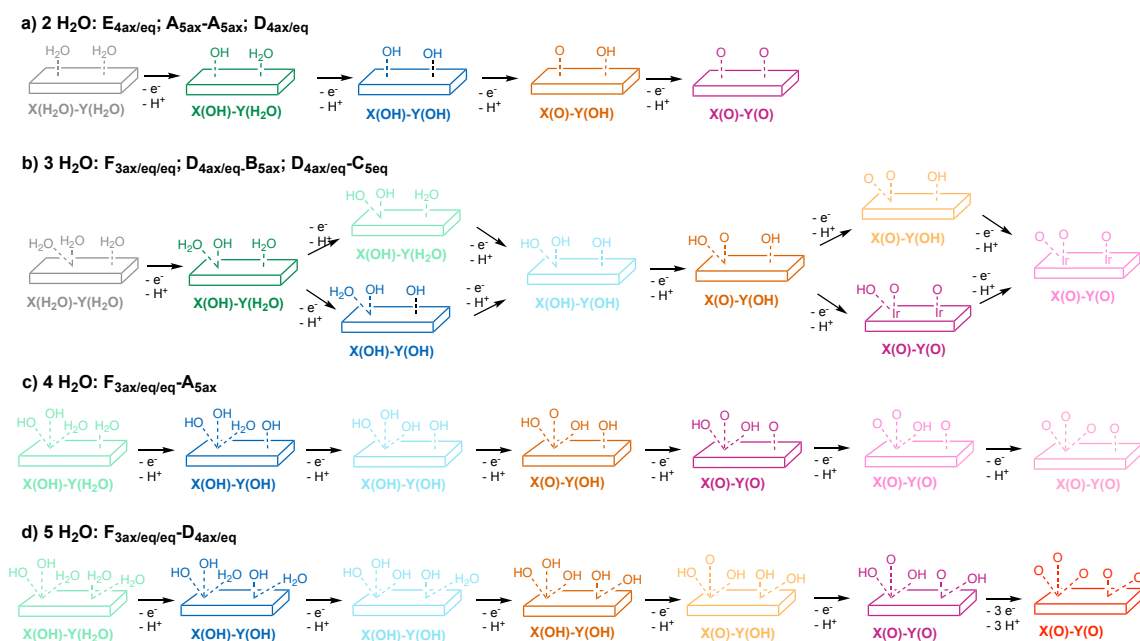
The results and discussion section is organized in two parts. We first focus on the oxidation of the surface iridium centers in presence of water as a function of the applied potential[61] and afterwards, we explore the OER reaction starting from the most stable species at 1.5 V, through either the I2M and WNA mechanisms. The choice for 1.5 V is based on the fact that this potential is close to the optimal value for performing the OER reaction with different Ir-based materials.[23,50,71]

3.1. Oxidation of surface Ir-(H₂O)_x. The oxidation of the six iridium centers of (IrO₂)₃₃ model (Figure 1) in the presence of water as a function of the applied potential have been analyzed with the aim of establishing the most stable structure at potentials around 1.5 V. Since we considered both the I2M and WNA mechanisms and the former path requires the participation of two Ir-O groups, the active site oxidation was modeled by considering either one single center that could lead to the formation of two oxo groups (**D_{4ax/eq}**, **E_{4eq/eq}** or **F_{3ax/eq/eq}**) or two vicinal iridium centers (**A_{5ax}-A_{5ax}**, **D_{4ax/eq}-B_{5ax}**, **D_{4ax/eq}-C_{eq}**, **F_{3ax/eq/eq}-A_{5ax}** or **F_{3ax/eq/eq}-D_{4ax/eq}**). The oxidation process takes place through several proton coupled electron transfer steps (PCET) and transforms the adsorbed water molecules to either Ir-OH or Ir-O species. The initial structure arises from adding one water molecule per vacant site in its preferred form (molecular or dissociated) as discussed in our previous contribution.[61] Then we considered the PCET processes until all metal centers present Ir-O species only. We explored all possibilities for the individual tri- and tetracoordinated sites and for systems involving two centers the combinations of the most stable structures of each site only. The optimized structures of the most stable isomers involved in the surface oxidation (Figures S1 to S8), the relative Gibbs energies between the different isomers of the intermediates involved in the oxidation process and the reaction Gibbs energies for all steps (Tables S1 to S15) are reported in the supplementary material.

Relative stabilities of the different species as a function of the applied potential were computed following equation 2



where $\mathbf{X(L_1)-Y(L_2)}$ stands for the oxidized species arising from $\mathbf{X(H_2O)-Y(H_2O)}$, n is the number of PCET processes required to go from $\mathbf{X(H_2O)-Y(H_2O)}$ to $\mathbf{X(L_1)-Y(L_2)}$ and U is the applied potential. Figure 2 summarizes the results. The color labeling indicates the most oxidized species in each center: i) grey indicates that all vacant sites are occupied by molecular or dissociated water molecules; ii) the green color indicates that at least one OH group as most oxidized species is present in one of the two considered centers; iii) the blue series accounts for structures with at least one OH group as most oxidized species at each iridium site; iv) orange color describes species with one Ir-O group in one of the metal centers and ; v) the pink colors indicate the presence of two Ir-O species (Scheme 2). According to our results on surface models,[56] the oxygen evolution catalysis requires the formation of species represented in pink in Figure 2, at around 1.5 V potentials.



Scheme 2.

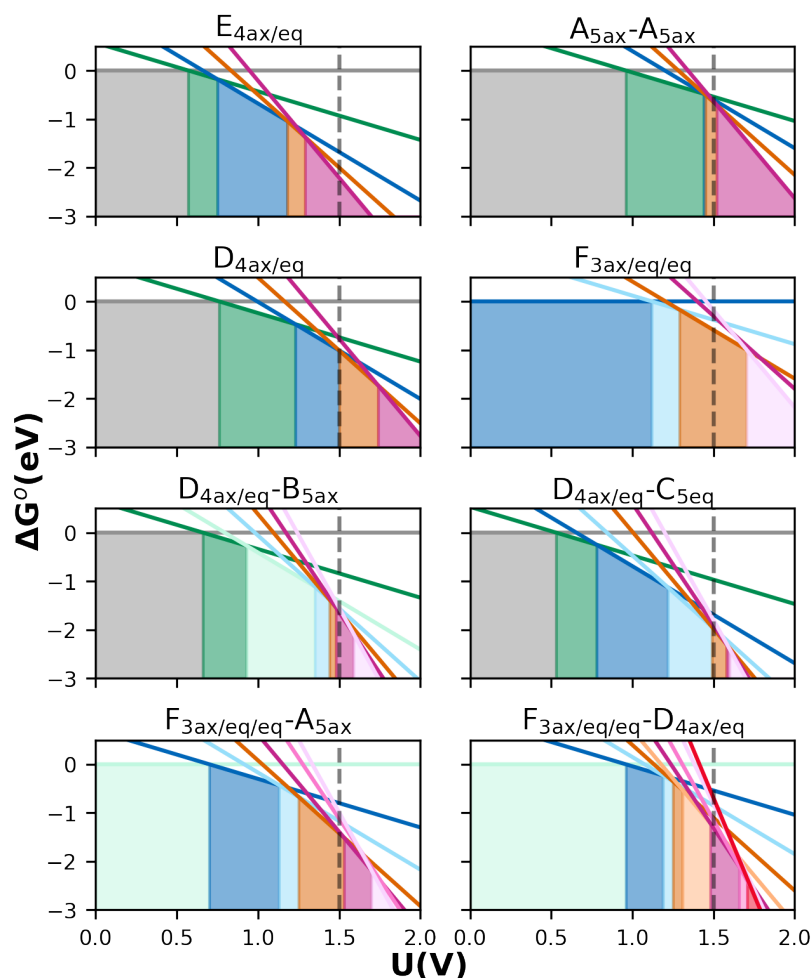


Figure 2. Phase diagram of the different sites of $(\text{IrO}_2)_{33}$ at $\text{pH} = 0$, $T = 298 \text{ K}$ and $P = 1 \text{ atm}$ as a function of the applied potential. Color labeling according to Scheme 2.

Results show that the required potential for the H_2O to OH oxidation is sensitive to the neighbor metal that is also being oxidized. The computed potentials for the H_2O to OH oxidation for one specific center can vary up to 0.2 eV and this appears to be related with the formation of hydrogen bonds. Centers able to establish strong hydrogen bonds with neighbor adsorbed species tend to present higher potentials for the H_2O to OH oxidation. However, this difference will likely be smaller if explicit solvent water molecules are added in the simulation due to the formation of hydrogen bonds between the adsorbed species and the solvent. Moreover, the H_2O to OH transition always takes

place at low potentials and thus this oxidation step does not appear to play a key role in the OER with iridium-based metals.

The Ir-OH to Ir-O oxidation is much less sensitive to the neighbor iridium center that it is being oxidized and this is related with the fact that Ir-OH species do not form strong hydrogen bonding with species adsorbed in the vicinity. Consequently, the values for each iridium center are essentially not affected by the nature of the other metal that it is being oxidized (< 0.08 eV). The formation of the first Ir-O species at tri- and tetraordinated iridium centers occurs at potentials between 1.18 and 1.50 V and the computed values tend to be lower than the required potentials for oxidizing pentacoordinated centers (between 1.45 and 1.54 V). Despite the small differences between the values, the general trend of the required potential for the formation of the first Ir-O species follows the order $E_{4eq/eq} < F_{3ax/eq/eq} < D_{4ax/eq} < A_{5ax} \sim B_{5ax} < C_{5eq}$ and this agrees with the observed trends for extended surface models.[56] Remarkably, the Ir-OH to Ir-O oxidation of the equatorial and axial sites of $D_{4ax/eq}$ with the other vacancy containing a Ir-OH group occurs at very similar potentials (difference of less than 0.03 V) and thus, both $D_{4eq/ax}(O/OH)$ and $D_{4eq/ax}(OH/O)$ structures should coexist.

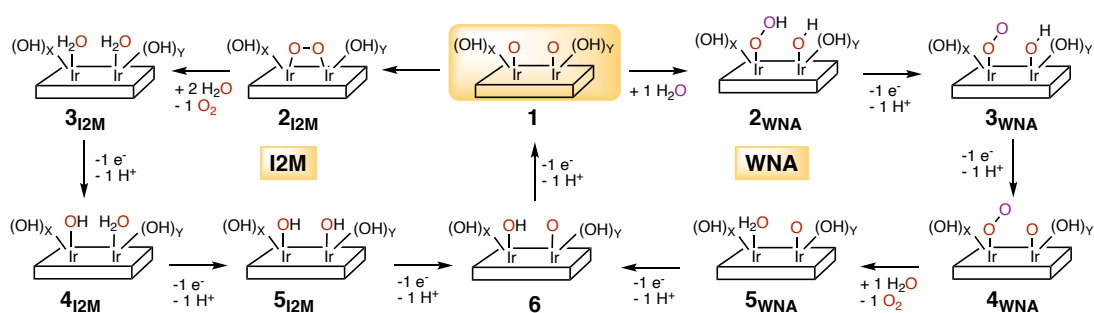
Full oxidation of the tri- and tetraordinated iridium centers ($D_{4eq/ax}$, $F_{3ax/eq/eq}$) requires high potentials (over 1.6 V). This suggests that at reaction conditions these centers will not be fully oxidized and they will remain as $Ir(O)(OH)_x$ ($x = 1$ or 2 for $D_{4eq/ax}$ and $F_{3ax/eq/eq}$ sites, respectively). $E_{4eq/eq}$ located at the tip of the nanoparticle is an exception. According to calculations, the full oxidation of this center occurs at 1.29 V and thus, it will present two Ir-O groups in one single iridium atom at reaction conditions as already found for the analogous centers of the (001) surface.[56] Overall, at 1.5 V the most

stable structures for all considered systems are: $D_{4ax/eq}(OH/O)$, $E_{4eq/eq}(O/O)$, $F_{3ax/eq/eq}(O/OH/OH)$, $A_{5ax}(O)-A_{5ax}(O)$, $D_{4ax/eq}(OH/O)-B_{5ax}(O)$, $D_{4ax/eq}(OH/O)-C_{5eq}(O)$, $F_{3ax/eq/eq}(O/OH/OH)-A_{5ax}(O)$ or $F_{3ax/eq/eq}(O/OH/OH)-D_{4ax/eq}(OH/O)$.

3.2. Oxygen evolution reaction catalytic activity. In a second step, we studied the OER reaction starting from the most stable structure at potentials around 1.5 V. We performed the study in the pairs of sites described above to have two Ir-O groups on the surface. We also considered $E_{4eq/eq}(O/O)$ that already has two oxyl species at 1.5 V. Despite being slightly less stable (less than 0.06 eV), we considered $D_{4ax/eq}(O/OH)-B_{5ax}(O)$ and $D_{4ax/eq}(O/OH)-C_{5eq}(O)$ instead of $D_{4ax/eq}(OH/O)-B_{5ax}(O)$ and $D_{4ax/eq}(OH/O)-C_{5eq}(O)$, since the OER reaction can only take place when the oxyl group is in the axial site (see Supplementary material). We considered the I2M and the WNA mechanisms shown in Scheme 3.

Noteworthy, and similarly to the mechanistic proposal made by other authors[50,55,58] for the OER on the IrO_2 (110) surface, we decoupled the water attack in two steps: i) the splitting of water over two Ir-O groups (**1** to **2_{WNA}** process in Scheme 3) and ii) a PCET process from the Ir-OOH/Ir-OH species (**2_{WNA}** to **3_{WNA}**). Another reaction mechanism where the water attack is coupled with the PCET has also been explored in the literature.[53] With the aim of analyzing the influence of the considered reaction mechanism, we also decided to consider this second possibility (see Table S15 of the supplementary material). We realized that the Ir-OOH/Ir-O species usually considered in this second route (**3'_{WNA}** in Scheme S1 of the supplementary material) is less stable than the Ir-OO/Ir-OH intermediate involved in the main mechanism reported here. This is in agreement with previous results on surfaces.[50,56] Moreover, similar results are

obtained for RuO₂ surfaces: the Ru-OO/Ru-OH intermediate is more stable than the Ru-OOH/Ru-O one and the geometrical features of the former matches with the experimental observations.[72] Therefore, it is very likely that regardless how the WNA process takes place (concerted or stepwise), the main intermediate involved in the O₂ formation is Ir-OO/Ir-OH rather than Ir-OOH/Ir-O. Comparison of the two approximations, assuming that the two routes involve the Ir-OO/Ir-OH species, suggests that the description of the WNA mechanism does not modify the general trends. Finally, since the two iridium centers are not equivalent in most of the pair of sites considered, there are two different WNA attack mechanisms depending on the iridium presenting the Ir-OOH species. We considered the two possibilities (WNA_x and WNA_y in Scheme S2 of the supplementary material), the associated Gibbs energies for each pathway are reported in Table S15 and the optimized structures of all species considered in the OER processes are shown in Figures S9-S24 of the supplementary material. The values reported in the text correspond to the most favorable pathway for each pair of sites. The ΔG values for the individual steps are reported in Table 1 and Figure 3 shows the global energy profile for the WNA mechanism.



Scheme 3.

The I2M mechanism starts with the coupling of two Ir-O species on the surface (**1** to **2_{I2M}** in Scheme 3 and Table 1). The process is in all cases endergonic, and the reaction Gibbs energies varies from 0.63 to 1.26 eV. These values tend to be slightly higher than those obtained with extended models,[56] although this may originate from the restrictions imposed for the optimizations with the nanoparticle models (See computational details). The energy cost for the O-O bond formation correlates reasonably well with the O···O distance in the initial structure (Table 1), since the more separated the oxygens initially are, the more unfavorable the process is. After O-O bond formation, O₂ release by adsorption of two water molecules is thermodynamically favorable (ΔG° between -0.92 and -1.33 eV) in all sites except at **E_{4eq/eq}**, where the reaction occurs in one single metal center. The catalytic cycle is closed through the oxidation of the adsorbed water species through processes that are equivalent to those described before and require potentials between 1.29 V and 1.58 V to recover the two Ir-O species. Overall, the I2M mechanism presents relatively low overpotentials (between 0.06 and 0.35 V). Indeed, these values are similar or even lower than those obtained for the WNA pathway (see below). However, the feasibility of the I2M mechanism is highly controlled by the oxo-coupling process, an endergonic chemical step whose reaction energies range between 0.63 eV and 1.26 eV.

Table 1. Reaction Gibbs Energies (in eV) for the chemical and electrochemical steps of the I2M and WNA reaction mechanisms. For those sites including Ir centers of different nature, only the most favorable pathway is reported. Reaction conditions are 0 V potential versus SHE, pH = 0, T = 298 K and P = 1 atm.

Reaction	$A_{5ax}-A_{5ax}$	$E_{4eq/eq}$	$D_{4ax/eq}-B_{5ax}$	$D_{4ax/eq}-C_{5eq}$	$F_{3ax/eq/eq}-A_{5ax}$	$F_{3ax/eq/eq}-D_{4ax/eq}$
I2M						
$1 \rightarrow 2_{I2M}$	0.81	0.80	0.63	1.02	1.17	1.26
$2_{I2M} + 2 H_2O \rightarrow 3_{I2M} + O_2$	-1.26	0.33	-0.92	-0.89	-0.36	-1.33
$3_{I2M} \rightarrow 4_{I2M} + H^+ + e^-$	0.96	0.57	0.93	0.55	0.55	1.38
$4_{I2M} \rightarrow 5_{I2M} + H^+ + e^-$	1.44	0.75	1.35	1.22	0.74	0.82
$5_{I2M} \rightarrow 6 + H^+ + e^-$	1.45	1.18	1.44	1.49	1.28	1.31
$6 \rightarrow 1 + H^+ + e^-$	1.52	1.29	1.49	1.58	1.53	1.48
WNA						
$1 + H_2O \rightarrow 2_{WNA}$	-0.53	0.47	-0.17	-0.27	0.09	-0.03
$2_{WNA} \rightarrow 3_{WNA} + H^+ + e^-$	1.31	0.88	1.19	1.01	0.93	1.16
$3_{WNA} \rightarrow 4_{WNA} + H^+ + e^-$	1.62	1.25	1.54	1.53	1.47	1.41
$4_{WNA} + H_2O \rightarrow 5_{WNA} + O_2$	-0.40	0.47	-0.11	0.44	0.26	-0.09
$5_{WNA} \rightarrow 6 + H^+ + e^-$	1.40	0.56	0.99	0.68	0.83	0.99
$6 \rightarrow 1 + H^+ + e^-$	1.52	1.29	1.48	1.52	1.34	1.48

Table 2. Ir-O_L distances (in Å) and spin moment for the most stable structures at working potentials.

Species	Ir ₁ -O ₁₁	Ir ₁ -O ₁₂	Ir ₁ -O ₁₃	Ir ₂ -O ₂₁	Ir ₂ -O ₂₂	O ₁ -O ₂ ^a	S _{O1} ^b	S _{O2} ^c	S _{Ir1}	S _{Ir2}
A_O-A_O	1.805			1.808		3.067	0.626	0.640	0.533	0.527
E_{O/O}	1.772	1.770			--	2.900	0.233/0.255		0.406	
D_{OH/O}	1.941	1.794			N/A		0.582		0.565	
D_{O/OH}-B_O	1.772	1.934		1.796		2.889	0.441	0.471	0.240	0.281
D_{O/OH}-C_O	1.939	1.794		1.950	1.804	4.434	0.587	0.698	0.582	0.532
F_{O/OH/OH}	1.778	1.917	1.930	1.804			0.314		0.314	
F_{O/OH/OH}-A_O-	1.776	1.916	1.931	1.787		3.249	0.412	0.646	0.389	0.538
F_{O/OH/OH}-D_{OH/O}	1.768	1.927	1.921	1.804		3.234	0.692	-0.242	0.700	-0.239

^a Distance between oxygens involved in the oxo-coupling step.^b Oxygen atom of the Ir-O species at Ir₁^c Oxygen atom of the Ir-O species at Ir₂

The WNA mechanism starts with the water attack to the two Ir-O of the surface, which leads to the formation of Ir-OOH and Ir-OH species (**1** to **2_{WNA}** in Scheme 3 and Table 1). The reaction Gibbs energies for this step varies from -0.53 to 0.47 eV, but in most cases the process is essentially isergonic. In general, the reaction Gibbs energies for the WNA step at the different sites of the nanoparticle and the values obtained with extended surface models are very similar and they all suggest that the process is easy. The sole exception is when the reaction takes place at **E_{4eq/eq}**. In this case, the process is unfavorable and the computed value ($\Delta G^{\circ}=0.47$ eV) is larger than that of the closely related (001) surface ($\Delta G^{\circ}=0.25$ eV).[56] However, comparison between the WNA reaction Gibbs energy (0.47 eV) and that for the O-O bond formation in the I2M mechanism (0.80 eV) in this **E_{4eq/eq}** site suggests that even in this case, the initial step for the WNA pathway is the preferred chemical step. Analysis of the spin densities over the oxygen atoms of Ir-O species (Table 2) shows that they have a marked oxyl radical character and thus, according to electronic density distribution, the water attack should be viewed as homolytic instead of nucleophilic. This is consistent with the fact that **E_{4eq/eq}** is the center presenting the lowest spin densities over the oxygen atoms.

After the O-O bond formation through the WNA mechanism, two PCET are required before O₂ is released (**2_{WNA}** \rightarrow **3_{WNA}** + 1H⁺ + 1e⁻ and **3_{WNA}** \rightarrow **4_{WNA}** + 1H⁺ + 1e⁻ in Scheme 3 and Table 1). For all centers, the **3_{WNA}** to **4_{WNA}** PCET is more challenging than the **2_{WNA}** to **3_{WNA}** one, the computed values being similar to those of the Ir-OH to Ir-O oxidation in the vicinity of a Ir-O group (**6** \rightarrow **1** + H⁺ + 1 e⁻ step). Thus, the potential determining step involves in all cases a Ir-OH to Ir-O oxidation and depending on the site, this step is either the **3_{WNA}** to **4_{WNA}** oxidation or the **6** to **1** process (Scheme 3 and Tables 1 and S17).

The resulting overpotentials are similar to those of the I2M pathway and range from 0.06 to 0.39 V.

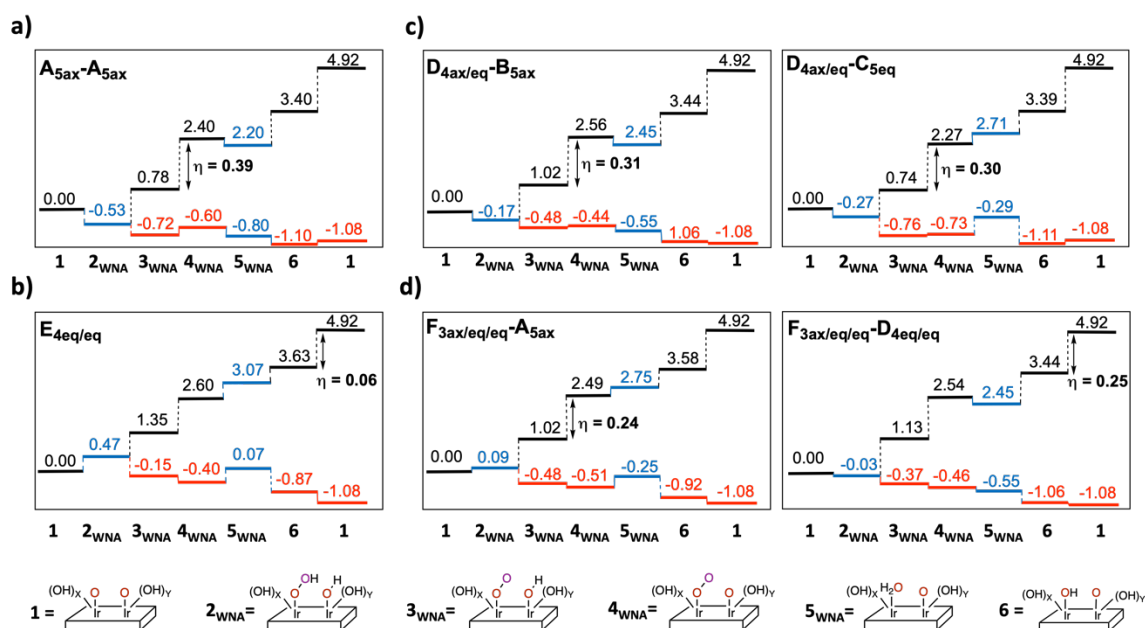


Figure 3. Calculated Gibbs energy profile for the most favorable OER catalytic cycle through the WNA mechanism at: a) the reference (110) sites of the nanoparticle; b) the tip site of the nanoparticle; c) sites including one penta and one tetra-coordinated metal center and d) sites including one tricoordinated site. The blue lines correspond to chemical steps, the black lines correspond to the energetics of the PCET at an applied potential of 0 V and the red values are for an applied potential of 1.5 V. Labelling taken from Figure 1 and Scheme 3.

Comparison between the O-O bond formation steps of the I2M and WNA mechanisms (Table 1) shows that the water attack is always more favorable than the oxo-coupling process. Moreover, the equivalent Gibbs energy barriers computed with different surface models show that the barriers are low and usually follow the same general trend as the thermodynamics of these individual steps.[50,56] In particular, for the WNA step, the ΔG^\ddagger values range from 0.42 to 0.55 eV in the main crystallographic facets. Therefore, assuming a similar value for the centers of the nanoparticle, the WNA will be preferred in all sites.

Consequently, the analysis of the overpotentials required to perform the reaction in each site is made by comparing the values of the WNA mechanism.

Figure 3 summarizes the Gibbs energies of the most favorable WNA pathway for the 6 different sites of the nanoparticle. It also reports the required overpotentials (η^{OER}) and outlines the potential determining step. The Figure is divided in four groups. **A_{5ax}-A_{5ax}** site, which corresponds to two iridium centers on the most stable (110) surface and thus, its reactivity is taken as the reference value (Figure 3a). The energetics associated with **E_{4eq/eq}**, which is the sole site involving only one iridium center, is shown in Figure 3b and those of all other sites, organized as function of the coordination number of the least saturated site, are given in Figure 3c for tetracoordinated metals and in Figure 3d for tricoordinated species. The computed overpotentials vary from 0.06 V to 0.39 V and they are mostly between 0.24 and 0.31 V. Despite the differences are small, the computed overpotential for the reference **A_{5ax}-A_{5ax}** site corresponds to the highest value (0.39 V). This suggest that most of the sites of the nanoparticle are more reactive than the sites on the most stable (110) surface. This agrees with the higher activity found for nanoparticles.[22–24] The case of **E_{4eq/eq}** is special: it presents the lowest overpotential (only 0.06 V) but the corresponding chemical processes are unfavorable, which could be detrimental in the final catalytic activity. Finally, the overpotentials computed for sites including one tetracoordinated metal as the least saturated center (**D_{4ax/eq}-B_{ax}** and **D_{4ax/eq}-C_{eq}**, Figure 3c) are larger than those computed for sites including initially tricoordinated iridium atoms (**F_{3ax/eq/eq}-A_{5ax}** and **F_{3ax/eq/eq}-D_{4ax/eq}**, Figure 3d) by 0.05 – 0.07 eV. The two groups show overpotentials that are lower to those of the **A_{5ax}-A_{5ax}** site of the (110) facet. This is indicative that centers that are initially bonded to the nanoparticle with a smaller number of bonds are more active. This correlates with the number of surface OH groups

at reaction conditions. Indeed, at working conditions it is expected that all vacant sites will be saturated with adsorbed species and according to the required overpotentials for the Iridium oxidation, this will mostly be OH groups. As a consequence, the tricoordinated metals present two OH groups on the surface and the tetracoordinated species, one single OH. Overall, our results suggest that the highest activity of IrO₂ nanoparticles when compared with crystalline materials and particularly the (110) facet arise from the higher activity of low coordinated sites. Remarkably, these low coordinated centers are likely more abundant on non-crystalline materials, thus suggesting that this could be one of the key factors for the highest activity of amorphous materials and, particularly, nanoparticles.[23,27,32]

4. CONCLUSIONS

Calculations on the oxygen evolution reaction catalytic activity of several iridium sites present on the (IrO₂)₃₃ Wulff-like stoichiometric nanoparticle model show that pentacoordinated sites located at the (110) surface are poorly active when compared to other centers of the nanoparticle. In contrast, tri- and tetracoordinated sites mainly located at tip, corner or edges (in larger models) of the nanoparticle present lower overpotentials. This suggests that these low coordinated sites are responsible for the higher catalytic activity observed for nanoparticles when compared to crystalline materials. These low coordinated sites are not fully oxidized at potentials around 1.5 V and the most stable structure at reaction conditions is Ir(O)(OH)_x (X = 1 or 2 for tetra- or tricoordinated centers, respectively). These low coordinated sites are likely more

abundant in amorphous materials, which can be one of the factors contributing to the higher catalytic activity of amorphous materials.

Funding. This work was supported by the Ministerio de Ciencia e Innovación, MICINN [PID2020-112715GB-I00], the Generalitat de Catalunya [2017SGR1323] and Red Española de Supercomputación [QCM-2019-1-0043, QS-2019-2-0031].

Supplementary material. The supplementary material includes the Gibbs energies of all structures considered in the oxidation process as function of the applied potential, the reaction Gibbs energies associated to the PCET steps of the site oxidation as function of the applied potential, the reaction Gibbs energies of all OER reaction mechanisms considered in this work and the Schemes defining these OER reaction mechanisms.

REFERENCES

- [1] L. Hammarström, *Acc. Chem. Res.* 42 (2009) 1859–1860.
- [2] S. Anantharaj, V. Aravindan, *Adv. Energy Mater.* 10 (2020) 1902666.
- [3] M.G. Walter, E.L. Warren, J.R. McKone, S.W. Boettcher, Q. Mi, E.A. Santori, N.S. Lewis, *Chem. Rev.* 110 (2010) 6446–6473.
- [4] X. Sala, S. Maji, R. Bofill, J. García-Antón, L. Escriche, A. Llobet, *Acc. Chem. Res.* 47 (2014) 504–516.
- [5] J.D. Blakemore, R.H. Crabtree, G.W. Brudvig, *Chem. Rev.* 115 (2015) 12974–13005.
- [6] B.M. Hunter, H.B. Gray, A.M. Müller, *Chem. Rev.* 116 (2016) 14120–14136.
- [7] J.H. Montoya, L.C. Seitz, P. Chakthranont, A. Vojvodic, T.F. Jaramillo, J.K. Nørskov, *Nat. Mater.* 16 (2017) 70–81.
- [8] C. Spöri, J.T.H. Kwan, A. Bonakdarpour, D.P. Wilkinson, P. Strasser, *Angew. Chemie Int. Ed.* 56 (2017) 5994–6021.
- [9] H. Ding, H. Liu, W. Chu, C. Wu, Y. Xie, *Chem. Rev.* 121 (2021) 13174–13212.
- [10] E. Fabbri, A. Habereder, K. Waltar, R. Kötz, T.J. Schmidt, *Catal. Sci. Technol.* 4 (2014) 3800–3821.
- [11] T. Reier, H.N. Nong, D. Teschner, R. Schlögl, P. Strasser, *Adv. Energy Mater.* 7 (2017) 1601275.
- [12] L. An, C. Wei, M. Lu, H. Liu, Y. Chen, G.G. Scherer, A.C. Fisher, P. Xi, Z.J. Xu, C. Yan, *Adv. Mater.* 33 (2021) 2006328.

- [13] C.C.L. McCrory, S. Jung, I.M. Ferrer, S.M. Chatman, J.C. Peters, T.F. Jaramillo, J. Am. Chem. Soc. 137 (2015) 4347–4357.
- [14] J. Yu, Q. He, G. Yang, W. Zhou, Z. Shao, M. Ni, ACS Catal. 9 (2019) 9973–10011.
- [15] D. Lebedev, R. Ezhov, J. Heras-Domingo, A. Comas-Vives, N. Kaeffer, M. Willinger, X. Solans-Monfort, X. Huang, Y. Pushkar, C. Copéret, ACS Cent. Sci. 6 (2020) 1189–1198.
- [16] J. Cheng, J. Yang, S. Kitano, G. Juhasz, M. Higashi, M. Sadakiyo, K. Kato, S. Yoshioka, T. Sugiyama, M. Yamauchi, N. Nakashima, ACS Catal. 9 (2019) 6974–6986.
- [17] H.N. Nong, T. Reier, H.-S. Oh, M. Gliech, P. Paciok, T.H.T. Vu, D. Teschner, M. Heggen, V. Petkov, R. Schlögl, T. Jones, P. Strasser, Nat. Catal. 1 (2018) 841–851.
- [18] D. Böhm, M. Beetz, M. Schuster, K. Peters, A.G. Hufnagel, M. Döblinger, B. Böller, T. Bein, D. Fattakhova-Rohlfing, Adv. Funct. Mater. 30 (2020) 1906670.
- [19] Q. Wang, Z. Zhang, C. Cai, M. Wang, Z.L. Zhao, M. Li, X. Huang, S. Han, H. Zhou, Z. Feng, L. Li, J. Li, H. Xu, J.S. Francisco, M. Gu, J. Am. Chem. Soc. 143 (2021) 13605–13615.
- [20] M. Ledendecker, S. Geiger, K. Hengge, J. Lim, S. Cherevko, A.M. Mingers, D. Göhl, G. V. Fortunato, D. Jalalpoor, F. Schüth, C. Scheu, K.J.J. Mayrhofer, Nano Res. 12 (2019) 2275–2280.
- [21] Y. Zhao, E.A. Hernandez-Pagan, N.M. Vargas-Barbosa, J.L. Dysart, T.E. Mallouk, J. Phys. Chem. Lett. 2 (2011) 402–406.
- [22] T. Reier, M. Oezaslan, P. Strasser, ACS Catal. 2 (2012) 1765–1772.

- [23] D.F. Abbott, D. Lebedev, K. Waltar, M. Povia, M. Nachtegaal, E. Fabbri, C. Copéret, T.J. Schmidt, *Chem. Mater.* 28 (2016) 6591–6604.
- [24] Y. Lee, J. Suntivich, K.J. May, E.E. Perry, Y. Shao-Horn, *J. Phys. Chem. Lett.* 3 (2012) 399–404.
- [25] P. Lettenmeier, L. Wang, U. Golla-Schindler, P. Gazdzicki, N.A. Cañas, M. Handl, R. Hiesgen, S.S. Hosseiny, A.S. Gago, K.A. Friedrich, *Angew. Chemie Int. Ed.* 55 (2016) 742–746.
- [26] L. Fu, X. Zeng, C. Huang, P. Cai, G. Cheng, W. Luo, *Inorg. Chem. Front.* 5 (2018) 1121–1125.
- [27] E. Oakton, D. Lebedev, M. Povia, D.F. Abbott, E. Fabbri, A. Fedorov, M. Nachtegaal, C. Copéret, T.J. Schmidt, *ACS Catal.* 7 (2017) 2346–2352.
- [28] R. Badam, M. Hara, H.-H. Huang, M. Yoshimura, *Int. J. Hydrogen Energy* 43 (2018) 18095–18104.
- [29] F. Bizzotto, J. Quinson, A. Zana, J.J.K. Kirkensgaard, A. Dworzak, M. Oezaslan, M. Arenz, *Catal. Sci. Technol.* 9 (2019) 6345–6356.
- [30] D. Lebedev, C. Copéret, *ACS Appl. Energy Mater.* 2 (2019) 196–200.
- [31] H. Jiang, S. Ge, Y. Zhang, M. Dong, S. Wu, M. Wu, J. Zhang, R. Ge, Z. Guo, *J. Phys. Chem. C* 124 (2020) 2–8.
- [32] P. Jovanovič, N. Hodnik, F. Ruiz-Zepeda, I. Arčon, B. Jozinovič, M. Zorko, M. Bele, M. Šala, V.S. Šelih, S. Hočevar, M. Gaberšček, *J. Am. Chem. Soc.* 139 (2017) 12837–12846.
- [33] R.M. Kluge, R.W. Haid, A.S. Bandarenka, *J. Catal.* 396 (2021) 14–22.

- [34] H. Dau, C. Limberg, T. Reier, M. Risch, S. Roggan, P. Strasser, *ChemCatChem* 2 (2010) 724–761.
- [35] E. Fabbri, T.J. Schmidt, *ACS Catal.* 8 (2018) 9765–9774.
- [36] S. Divanis, T. Kutlusoy, I.M. Ingmer Boye, I.C. Man, J. Rossmeisl, *Chem. Sci.* 11 (2020) 2943–2950.
- [37] O. Piqué, F. Illas, F. Calle-Vallejo, *Phys. Chem. Chem. Phys.* 22 (2020) 6797–6803.
- [38] K.A. Stoerzinger, O. Diaz-Morales, M. Kolb, R.R. Rao, R. Frydendal, L. Qiao, X.R. Wang, N.B. Halck, J. Rossmeisl, H.A. Hansen, T. Vegge, I.E.L. Stephens, M.T.M. Koper, Y. Shao-Horn, *ACS Energy Lett.* 2 (2017) 876–881.
- [39] M. García-Melchor, L. Vilella, N. López, A. Vojvodic, *ChemCatChem* 8 (2016) 1792–1798.
- [40] K. Klyukin, A. Zagalskaya, V. Alexandrov, *J. Phys. Chem. C* 122 (2018) 29350–29358.
- [41] L.C. Seitz, C.F. Dickens, K. Nishio, Y. Hikita, J. Montoya, A. Doyle, C. Kirk, A. Vojvodic, H.Y. Hwang, J.K. Norskov, T.F. Jaramillo, *Science* 353 (2016) 1011–1014.
- [42] G. Buvat, M.J. Eslamibidgoli, A.H. Youssef, S. Garbarino, A. Ruediger, M. Eikerling, D. Guay, *ACS Catal.* 10 (2020) 806–817.
- [43] J. Gao, C.-Q. Xu, S.-F. Hung, W. Liu, W. Cai, Z. Zeng, C. Jia, H.M. Chen, H. Xiao, J. Li, Y. Huang, B. Liu, *J. Am. Chem. Soc.* 141 (2019) 3014–3023.
- [44] W. Sun, Z. Wang, W.Q. Zaman, Z. Zhou, L. Cao, X.-Q. Gong, J. Yang, *Chem. Commun.* 54 (2018) 996–999.

- [45] J. Rossmeisl, Z.-W. Qu, H. Zhu, G.-J. Kroes, J.K. Nørskov, *J. Electroanal. Chem.* 607 (2007) 83–89.
- [46] Z. Xu, J. Rossmeisl, J.R. Kitchin, *J. Phys. Chem. C* 119 (2015) 4827–4833.
- [47] S. Siahrostami, A. Vojvodic, *J. Phys. Chem. C* 119 (2015) 1032–1037.
- [48] I.C. Man, H. Su, F. Calle-Vallejo, H.A. Hansen, J.I. Martínez, N.G. Inoglu, J. Kitchin, T.F. Jaramillo, J.K. Nørskov, J. Rossmeisl, *ChemCatChem* 3 (2011) 1159–1165.
- [49] Y.-H. Fang, Z.-P. Liu, *J. Am. Chem. Soc.* 132 (2010) 18214–18222.
- [50] Y. Ping, R.J. Nielsen, W.A. Goddard, *J. Am. Chem. Soc.* 139 (2017) 149–155.
- [51] J.A. Gauthier, C.F. Dickens, L.D. Chen, A.D. Doyle, J.K. Nørskov, *J. Phys. Chem. C* 121 (2017) 11455–11463.
- [52] L.G. V. Briquet, M. Sarwar, J. Mugo, G. Jones, F. Calle-Vallejo, *ChemCatChem* 9 (2017) 1261–1268.
- [53] C.F. Dickens, C. Kirk, J.K. Nørskov, *J. Phys. Chem. C* 123 (2019) 18960–18977.
- [54] A. Zagalskaya, V. Alexandrov, *J. Phys. Chem. Lett.* 11 (2020) 2695–2700.
- [55] H.N. Nong, L.J. Falling, A. Bergmann, M. Klingenhof, H.P. Tran, C. Spöri, R. Mom, J. Timoshenko, G. Zichittella, A. Knop-Gericke, S. Piccinin, J. Pérez-Ramírez, B.R. Cuenya, R. Schlögl, P. Strasser, D. Teschner, T.E. Jones, *Nature* 587 (2020) 408–413.
- [56] D. González, J. Heras-Domingo, M. Sodupe, L. Rodríguez-Santiago, X. Solans-Monfort, *J. Catal.* 396 (2021) 192–201.
- [57] A. Halder, C. Liu, Z. Liu, J.D. Emery, M.J. Pellin, L.A. Curtiss, P. Zapol, S. Vajda,

- A.B.F. Martinson, *J. Phys. Chem. C* 122 (2018) 9965–9972.
- [58] K. Bhattacharyya, C. Poidevin, A.A. Auer, *J. Phys. Chem. C* 125 (2021) 4379–4390.
- [59] D. González, B. Camino, J. Heras-Domingo, A. Rimola, L. Rodríguez-Santiago, X. Solans-Monfort, M. Sodupe, *J. Phys. Chem. C* 124 (2020) 1227–1237.
- [60] D. González, J. Heras-Domingo, S. Pantaleone, A. Rimola, L. Rodríguez-Santiago, X. Solans-Monfort, M. Sodupe, *ACS Omega* 4 (2019) 2989–2999.
- [61] D. González, M. Sodupe, L. Rodríguez-Santiago, X. Solans-Monfort, *Nanoscale* 13 (2021) 14480–14489.
- [62] G. Kresse, J. Furthmüller, *Phys. Rev. B* 54 (1996) 11169–11186.
- [63] G. Kresse, J. Hafner, *Phys. Rev. B* 47 (1993) 558–561.
- [64] J.P. Perdew, K. Burke, M. Ernzerhof, *Phys. Rev. Lett.* 77 (1996) 3865–3868.
- [65] S. Grimme, *J. Comput. Chem.* 25 (2004) 1463–1473.
- [66] Y. Ping, G. Galli, W.A. Goddard, *J. Phys. Chem. C* 119 (2015) 11570–11577.
- [67] G. Kresse, D. Joubert, *Phys. Rev. B* 59 (1999) 1758–1775.
- [68] P.E. Blöchl, *Phys. Rev. B* 50 (1994) 17953–17979.
- [69] K. Mathew, R. Sundararaman, K. Letchworth-Weaver, T.A. Arias, R.G. Hennig, *J. Chem. Phys.* 140 (2014) 084106.
- [70] J.K. Nørskov, J. Rossmeisl, A. Logadottir, L. Lindqvist, J.R. Kitchin, T. Bligaard, H. Jónsson, *J. Phys. Chem. B* 108 (2004) 17886–17892.
- [71] H.N. Nong, L. Gan, E. Willinger, D. Teschner, P. Strasser, *Chem. Sci.* 5 (2014)

2955–2963.

- [72] R.R. Rao, M.J. Kolb, L. Giordano, A.F. Pedersen, Y. Katayama, J. Hwang, A. Mehta, H. You, J.R. Lunger, H. Zhou, N.B. Halck, T. Vegge, I. Chorkendorff, I.E.L. Stephens, Y. Shao-Horn, *Nat. Catal.* 3 (2020) 516–525.

Graphical abstract

